Level-S^{2}fM: Structure from Motion on Neural Level Set of Implicit Surfaces

Yuxi Xiao[1] Nan Xue[1*] Tianfu Wu[2] Gui-Song Xia[1]
[1] Wuhan University [2] NC State University

Abstract

This paper presents a neural incremental Structure-from-Motion (SfM) approach, Level-S^{2}fM. In our formulation, we aim at simultaneously learning coordinate MLPs for the implicit surfaces and the radiance fields, and estimating the camera poses and scene geometry, which is mainly sourced from the established keypoint correspondences by SIFT. Our formulation would face some new challenges due to inevitable two-view and few-view configurations at the beginning of incremental SfM pipeline for the optimization of coordinate MLPs, but we found that the strong inductive biases conveying in the 2D correspondences are feasible and promising to avoid those challenges by exploiting the relationship between the ray sampling schemes used in volumetric rendering and the sphere tracing of finding the zero-level set of implicit surfaces. Based on this, we revisit the pipeline of incremental SfM and renew the key components of two-view geometry initialization, the camera pose registration, and the 3D points triangulation, as well as the Bundle Adjustment in a novel perspective of neural implicit surfaces. Because the coordinate MLPs unified the scene geometry in small MLP networks, our Level-S^{2}fM treats the zero-level set of the implicit surface as an informative top-down regularization to manage the reconstructed 3D points, reject the outlier of correspondences by querying SDF, adjust the estimated geometries by NBA (Neural BA), finally yielding promising results of 3D reconstruction. Furthermore, our Level-S^{2}fM alleviated the requirement of camera poses for neural 3D reconstruction.

1. Introduction

Structure-from-Motion (SfM) is a fundamental 3D vision problem that aims at reconstructing 3D scenes and estimating the camera motions from a set of uncalibrated images. As a long-standing problem, there have been a tremendous of studies that are mostly established on the keypoint correspondences across viewpoints and the theoretical findings of Multi-View Geometry (MVG) [12], and have formed three representative pipelines of Incremental SfM [34], Global SfM [4, 45], and Hybrid SfM [5].

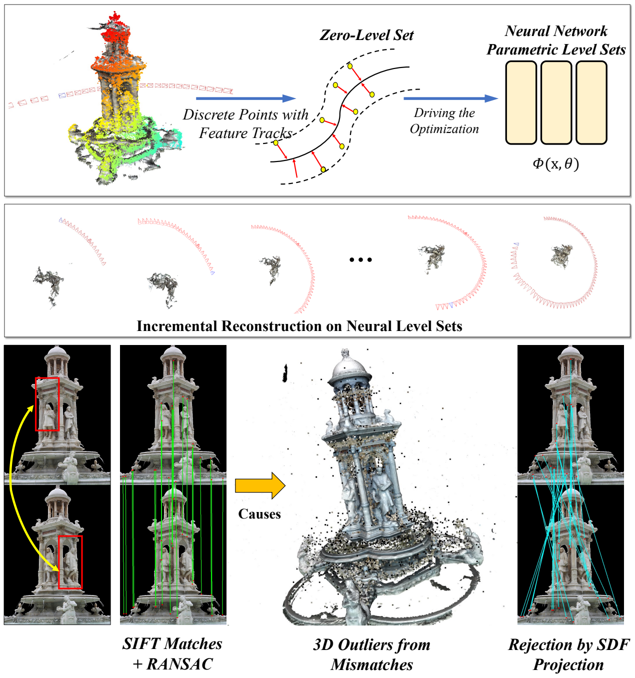
Zero-Level Set
Neural Network Parametric Level Sets
Discrete Points with Feature Tracks
Driving the Optimization
$\Phi(x, \theta)$
...
Incremental Reconstruction on Neural Level Sets
Causes
SIFT Matches + RANSAC
3D Outliers from Mismatches
Rejection by SDF Projection

Figure 1. **SfM calculations on neural level sets.** We learn to do the geometric calculations including Triangulation, PnP and Bundle Adjustment above neural level sets, which easily help to reject the outliers in the matches especially in the texture repeated scenes. Also, due to the continuous surface priors of neural level sets, we achieve better pose estimation accuracy and our reconstructed points are sticking on the surface which are painted with color in the figure. While, there are a lot of outlier 3d points reconstructed by COLMAP [34] which are painted by black.

In this paper, we focus on the incremental pipeline of SfM and we will use SfM to refer to the incremental SfM. Given an unordered image set, an SfM system initializes the computation by a pair of images that are with well-conditioned keypoint correspondences to yield an initial set of feature tracks, then incrementally adds new views one by one to estimate the camera pose from the 2D-3D point correspondences and update the feature tracks with new matches. Because the feature tracks are generated by grouping the putative 2D correspondences across viewpoints in

[*] Corresponding Author

bottom-up manners, they would be ineffective or inaccurate to represent holistic information of scenes. Accordingly, Bundle Adjustment (BA) is necessary to jointly optimize the camera poses and 3D points in a top-down manner. The success of BA indicates that a global perspective is vital for accurate 3D reconstruction, however, their input feature tracks are the bottom-up cues without enough holistic constraints for the 3D scenes. To this end, we study to integrate the top-down information into the SfM system by proposing a novel SfM solution, called Level-S^{2}fM. Fig. 1 illustrates a representative case for the classic SfM systems that will yield more flying 3D scene points, which can be addressed by our method.

Our Level-S^{2}fM is inspired by the recently-emerged neural implicit surface that could manage all 3D scene points as the zero-level set of the signed distance function (SDF). Because the neural implicit surfaces can be parameterized by Multi-Layer Perceptrons (MLPs), it could be viewed as a kind of top-down information of 3D scenes and is of great potential for accurate 3D reconstruction. However, because both the 3D scene and camera poses are to be determined, it poses a challenging problem:

> *How can we optimize an implicit neural SDF (or other neural fields such as NeRF) from only a set of uncalibrated images without any 3D information?*

Most recently, the above problem was partially answered in BARF [19] and NeRF-- [44] that relaxed the requirement of optimizing Neural Radiance Fields [25] without knowing accurate camera poses, but they can only handle the unknown pose configurations in small-scale *face-forwarding* scenes. Moreover, when we confine the problem in the incremental SfM pipelines, it would be more challenging as we need to optimize the neural fields with only two overlapped images at the initialization stage. To this end, we found that the optimization of neural SDF can be accomplished by the 2D matches at the initialization stage, and facilitate the management of feature tracks by querying the 3D points and tracing the 2D keypoints in a holistic way.

As shown in Fig. 1, we define a neural network that parameterizes an SDF as the unified representation for the underdetermined 3D scene and accomplishes the computations of PnP for camera pose intersection, the 3D points triangulation as well as the geometry refinement on the parameterized SDF. In the initialization stage with a pair of overlapped images, Level-S^{2}fM uses the differentiable sphere tracing algorithm [20] to attain the corresponding 3d points of the keypoints and calculate the reprojection error to drive the joint optimization. For the traced 3d points with small SDF values and 2D reprojection errors for its feature track, they are added into a dynamic point set and take the point set with feature tracks as the Lagrangian representation for the level sets. Because the pose estimation and the scene points reconstruction are sequentially estimated, the estimation errors will be accumulated. To this end, we present an NBA (*i.e*., Neural Bundle Adjustment) that plays a similar role as in Bundle Adjustment, but it optimizes the implicit surface and camera poses from the explicit flow of points by the energy function of the reprojection errors, which can be viewed as an evolutionary step between Lagrangian and Eulerian representations as discussed in [24].

In the experiments, we comprehensively evaluate our Level-S^{2}fM on a variety of scenes from two datasets [15, 46]. On the BlendedMVS dataset, our proposed Level-S^{2}fM clearly outperforms the state-of-the-art COLMAP [34] by significant margins. In particular, our method averagely reduced the rotation error by 55 percentages from 1.54° to 0.86°. For the reconstructed scene geometry, our Level-S^{2}fM reduced the ACC from 3.16cm to 2.25cm, obtaining a relative improvement of 28%. On the DTU dataset [15], our method also obtains on-par performance with COLMAP for both camera pose estimation and dense surface reconstruction, which are all computed in one stage.

The contributions of this paper are in two folds:

- We present a novel neural SfM approach Level-S^{2}fM, which formulates to optimize the coordinate MLP networks for implicit surface and radiance field and estimate the camera poses and scene geometry. To the best of our knowledge, our Level-S^{2}fM is the first implicit neural SfM solution on the zero-level set of surfaces.

- From the perspective of neural implicit field learning, we show that the challenging problems of two-view and few-view optimization of neural implicit fields can be addressed by exploiting the inductive biases conveyed in the 2D correspondences.

2. Related Works

2.1. Structure from Motion

There has been a vast body of literature on Structure from Motion. Since an SfM system consists of many components, tremendous efforts have been devoted to improving the core components of SfM. In particular, the learning techniques were introduced in a variety of subproblems including image matching [7, 33], feature track mining and management [41], two-view 3D reconstruction [40], relative and absolute camera pose estimation [14] and Bundle Adjustment [3, 39]. Those studies indicated that the learning paradigms are promising to improve the quality of 3D reconstruction. However, to the best of our knowledge, the learning paradigms are not fully equipped in SfM systems. One possible reason for such a fact is that the many learning approaches are designed in a supervised learning fashion, which remains some risks on the out-of-distribution samples. The self-supervised learning approaches [9, 23] in 3D vision alleviated the requirement of data annotations, however, they have not been fully exploited in the whole pipeline of SfM. In contrast to the aforementioned studies, in this paper, we are interested in integrating the learning ability into the SfM system without incurring any external data annotations. From the perspective of system design in SfM, we verified that the strong inductive biases conveying in the 2D correspondences are promising and meaningful to drive the learning and optimization of SfM.

2.2. Neural Implicit Representation for 3D Scene

Recently, the advent of neural implicit fields [25, 30, 31, 42, 43, 47] have greatly advanced many 3D vision problems such as novel-view synthesis [1, 25] and surface reconstruction [30, 31, 42, 47] by learning to optimize the coordinate MLPs from a set of posed RGB images of which the key to success is that the inductive biases of 3D are exploited by the neural networks. However, when the camera poses are invalid, it is hard to optimize the coordinate MLPs for neural implicit fields. To remedy this, the state-of-the-art SfM system, COLMAP [34], is extensively used to compute the camera poses as a preprocessing step.

To train the neural field from unknown poses directly, recently, BARF [19] and NeRF [44] explored to jointly optimize the camera poses and neural fields by the volumetric rendering with promising results obtained in forward-facing scenes. BARF can also work in some scenes of highly overlapped and dense image collections with the initialized poses as inputs. This problem was also studied in the RGB-D SLAM systems [2, 38, 48], however, their works mainly rely on the known depth information and focus on the camera pose tracking by the neural implicit fields. Therefore, how to optimize implicit neural fields from only a set of uncalibrated images without any 3D information input is still a challenging and open problem.

In this paper, we study the unknown-pose neural fields optimization and SfM together and present a unified solution that simultaneously learns the implicit surfaces and radiance fields alongside the camera pose estimation and scene reconstruction from a set of images.

3. Preliminaries

In this section, we introduce the preliminaries on neural implicit surface rendering and the notations in SfM, which are all extensively used in our method.

3.1. Neural Implicit Surface Rendering

The volumetric rendering of neural implicit surface [47] aims at learning a signed distance function $d_\Omega : \mathbb{R}^3 \to \mathbb{R}$ by the volumetric rendering from a set of posed images and then extracting the zero-level set of ϕ as the reconstructed surface model of the image set. The state-of-the-art approach, VolSDF [47], integrates SDF representations with neural volume rendering via Laplacian distribution by

$$\sigma(\mathbf{x}) = \frac{1}{\beta}\Psi_\beta(-d_\Omega(\mathbf{x})), \tag{1}$$

where β is a learnable parameter in VolSDF [47]. Based on Eq. (1), the volume rendering equation renders a ray $\mathbf{x}(t)$ emanating from a camera position $\mathbf{o} \in \mathbb{R}^3$ in unit direction $\mathbf{v}$, defined by $\mathbf{x}(t) = \mathbf{o} + t\mathbf{v}$ by

$$I(\mathbf{o}, \mathbf{v}) = \int_0^\infty L(\mathbf{x}(t), \mathbf{n}(t), \mathbf{v})\sigma(\mathbf{x}(t))T(t)dt, \tag{2}$$

where $L(\mathbf{x}, \mathbf{n}, \mathbf{v})$ is the radiance field and $\mathbf{n}(t)$ is the normal direction of the point $\mathbf{x}(t)$ defined by $\mathbf{n}(t) = \nabla_\mathbf{x} d_\Omega(\mathbf{x}(t))$. In the learning of volume rendering, two coordinate MLP (Multi-Layer Perceptron) networks parameterize the SDF by $\phi(\mathbf{x}) = (d(\mathbf{x}), \mathbf{z}(\mathbf{x})) \in \mathbb{R}^{1+256}$ and the radiance field by $L_\psi(\mathbf{x}, \mathbf{n}, \mathbf{v}, \mathbf{z}) \in \mathbb{R}^3$, and train them by the color loss $\mathcal{L}_{\mathrm{RGB}}(\phi, \psi, \beta)$ and the Eikonal loss $\mathcal{L}_{eik}(\phi) = \mathbb{E}_\mathbf{z}(|\nabla d(\mathbf{z})\| - 1)$.

In this paper, we use the equations (1) and (2) as the basic tools for Level-S^{2}fM. To make the optimization of SDF and radiance networks easier, we set β as a small constant number and use the multi-resolution grid representations to avoid the potential of slow convergence and catastrophic forgetting since the scene scale is unknown and the original VolSDF [47] requires to normalize the known camera poses in a certain scale.

3.2. Ray Sampling and Sphere Tracing

Iterative Ray Sampling. In the implementation, the continuous form of Eq. (2) is approximated in

$$I(\mathbf{o}, \mathbf{v}) \approx \sum_{i=1}^{m-1} \hat{\tau}_i L(\mathbf{x}(t_i), \mathbf{n}(t_i), \mathbf{v}), \tag{3}$$

where $\{t_i\}_{i=1}^m$ is the discrete samples, $0 = t_1 < t_2 < \ldots < t_m = M$, M is some large constant. $\hat{\tau}_i \approx \tau(s_i)\Delta s$ is the approximated PDF multiplied by the interval length. In VolSDF [47], $\{t_i\}_{i=1}^m$ is adaptively computed according to the opacity approximation error. Please move to [47] for its detail. In our method, we keep using this iterative sampling strategy when the rendering loss and the Eikonal loss is used. However, because the sampling set $\{t_i\}$ would be large, we do not use this strategy to compute the 3D points from 2D keypoints in our Level-S^{2}fM and in turn to use the sphere tracing [10] as a faster way since our initial development of this work.

Sphere Tracing. Sphere tracing is a geometric method to render the depth from a signed distance function. Different from iterative ray sampling, sphere tracing is designed to hit the surface point along the ray $\mathbf{x}(t)$ with queries as few as possible. To make it clear, we use s_i to denote the ray stamp of the queried point $\mathbf{x}(s_i)$. With the queried point $\mathbf{x}(s_i)$, the next ray stamp s_{i+1} is computed by $s_{i+1} = \phi(\mathbf{x}(s_i))$. In our study, we sample at most $N_s = 20$ points with the stop criterion $|\phi(s_i)| < \varepsilon$, where ε is set to 0.002 in our experiment.

Remarks. Although both the iterative ray sampling [47] and sphere tracing [10] share the same target of computing the surface point along a ray, they have different behaviors in the neural implicit surface optimization. In detail, because VolSDF [47] aims at approximating the opacity by SDF, it updates the SDF network $\phi(\mathbf{x})$ by the rendering loss $\mathcal{L}_{\text{color}}$. As for sphere tracing, it is a geometric approach that only takes the SDF values into account for the computation. Such a difference is trivial to some extent, however, we found that their different focuses induce a loss function in our Level-S^{2}fM to constraint the rendered depth values (or 3D points) for two-view initialization and 3D point triangulation.

3.3. Notations in SfM

Correspondence Search. Given the image set $\mathcal{I} = \{I_i | i = 1 \dots N_I\}$ for reconstruction, the keypoint features of the image I_i computed by SIFT [22] is denoted in $\mathcal{F}_i = \{(x_j, \mathbf{f}_j)\}$, where $x_j \in \mathbb{R}^2$ is the 2D coordinate and $\mathbf{f}_j \in \mathbb{R}^{128}$ is the feature descriptor of x_j. Based on the SIFT features, we follow the schema in COLMAP [34] to establish the feature correspondences across views, in which we first do the exhaustive matching for all possible image pairs and then use the geometric verification to filter out the non-overlapped image pairs. After this, the potentially overlapped image pairs are denoted in $\mathcal{C} = \{(I_a, I_b) | I_a, I_b \in \mathcal{I}\}$, and the keypoint correspondences in the pair (I_a, I_b) are denoted in the set $\mathcal{M}_{ab} = \{\{(x_k, \mathbf{f}_k), (x'_l, \mathbf{f}'_l)\} \,|(x_k, \mathbf{f}_k \in \mathcal{F}_a, (x'_l, f'_l) \in \mathcal{F}_b\}$. Finally, all the prepared correspondences are organized as the scene graph [34, 36], which stores images as the graph nodes and the overlapped image pairs as the graph edges. In our Level-S^{2}fM, we use the established correspondences to drive the learning of MLPs, estimate the camera poses, and reconstruct a sparse point set of correspondences.

3D Scene Points and Feature Tracks. Because SfM is designated to simultaneously estimate the scene geometry from 2D correspondences, every successfully reconstructed 3D scene point is sourced from multiple 2D keypoint observations. To facilitate the representation, we denote the expected 3D point set in $\mathcal{X} = \{\mathbf{X}_k \in \mathbb{R}^3 | k = 1, \dots, N_{3d}\}$. For each point $\mathbf{X}_k \in \mathcal{X}$, if it is reconstructed from the 2D keypoint $x_j \in \mathcal{F}_i$, we denote such a relationship in a tuple (k, i, j). The set $\mathcal{T} = \{(k, i, j)\}$ is called the set of feature tracks.

4. The Proposed Level S^{2}fM

In this section, we present the details of our Level-S^{2}fM. As shown in Fig. 2, our method consists of three classical components including 1) the two-view geometry initialization, 2) the new frame registration, and 3) the new frame pose refinement, an implicit surface and a radiance field that are parameterized by neural networks. In what follows, we will show how to solve the SfM problem by learning the implicit fields with 2D correspondences. We assume the intrinsic matrix K is known and fixed.

4.1. Two-view Initialization

We first select two good views $\{I_a, I_b\}$ for initialization from the scene graph and get their 2D matches $\mathcal{M}_{ab} = \{\{(x_k, \mathrm{f_k}), (x_l^{'}, \mathrm{f}_l^{'})\} | (x_k, \mathrm{f_k}) \in \mathcal{F}_a, (x_l^{'}, \mathrm{f}_l^{'}) \in \mathcal{F}_b\}$. Based on the 2D matches $\mathcal{M}_{ab}$, we leverage the 5-point algorithm [29] and RANSAC to obtain the poses $P_a, P_b \in SE(3)$.

With the estimated camera poses P_a, P_b, it is straightforward to optimize the SDF network $\phi(\mathbf{x})$ and the radiance field network $L_\psi(\mathbf{x}, \mathbf{n}, \mathbf{v}, \mathbf{z})$ defined in Sec. 3 by minimizing the loss items $\mathcal{L}_{\text{RGB}}$ and $\lambda\mathcal{L}_{eik}$ as done in VolSDF [47]. However, it should be noted that the learning of volumetric surface rendering in such a way for the **two-view inputs** would trap into the local minimal by overfitting. To this end, we propose to use the differentiable sphere tracking [10, 20] for the corresponding rays in image I_a and I_b, which provides strong inductive biases for the optimization of networks.

Specifically, denoted by a pair of feature match (x_k, x'_l) in the image pair (I_a, I_b), the sphere tracing obtains the surface point $\mathbf{X}_a^k = \mathbf{o}_a + \hat{t}_a \mathbf{d}_a$ from the SDF and $\mathbf{X}_b^l = \mathbf{o}_b + \hat{t}_b \mathbf{d}_b$, where $(\mathbf{o}_a, \mathbf{d}_a)$ is the ray of x_k, $(\mathbf{o}_b, \mathbf{d}_b)$ is the ray of x'_l. For the computation of $\hat{t}_a$ and $\hat{t}_b$, please move to our supplementary materials. Ideally, the $\mathbf{X}_a^k$ and $\mathbf{X}_b^l$ should be as close as possible, therefore, we introduce a reprojection loss

$$\mathcal{L}_{\text{reproj}} = \frac{1}{2V} \sum (\|\hat{x}_k - x'_l\|_2 + \|\hat{x}'_l - x_k\|_2), \tag{4}$$

where V is the number of correspondences, $\hat{x}_k = \Pi(\mathbf{X}_a^k, K, P_b)$ and $\hat{x}'_l = \Pi(\mathbf{X}_b^l, K, P_a)$ are the projected 2D coordinates of the traced 3D points by the projection Π.

Considering the fact that the correspondences are sparse when the SDF network is not well optimized at some rays, the sparse sample points by sphere tracing on the SDF network may be either inaccurate or erroneous as shown in Fig. 3. Therefore, we use a depth consistency loss $\mathcal{L}_{dc}$ to minimize the depth estimated by the sphere tracing and the

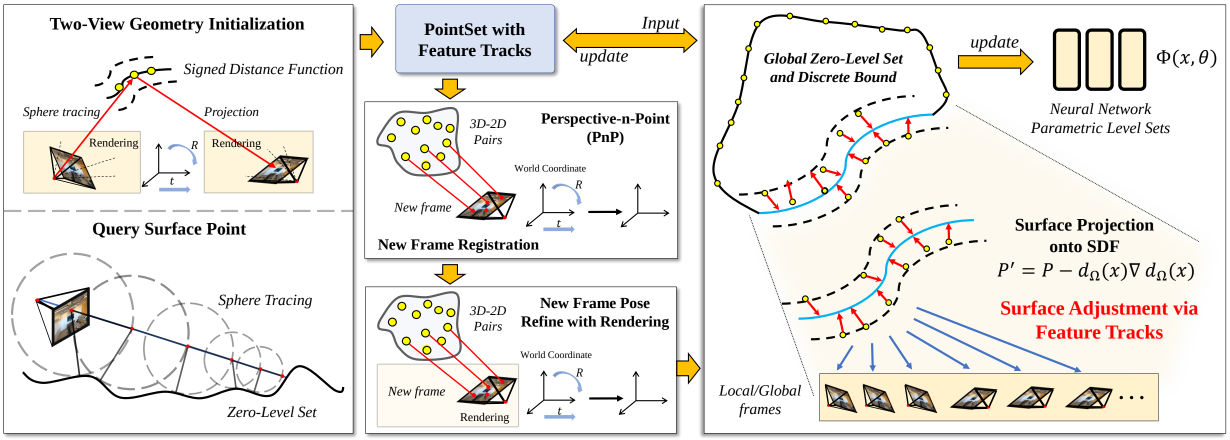
Two-View Geometry Initialization
Signed Distance Function
Sphere tracing
Projection
Rendering
R
t
Rendering
Query Surface Point
Sphere Tracing
Zero-Level Set
PointSet with Feature Tracks
Input
update
3D-2D Pairs
Perspective-n-Point (PnP)
World Coordinate
R
New frame
t
New Frame Registration
3D-2D Pairs
New Frame Pose Refine with Rendering
World Coordinate
R
New frame
Rendering
t
Global Zero-Level Set and Discrete Bound
update
$\Phi(x,\theta)$
Neural Network Parametric Level Sets
Surface Projection onto SDF
$P' = P - d_\Omega(x)\nabla\, d_\Omega(x)$
Surface Adjustment via Feature Tracks
Local/Global frames
...

Figure 2. **Overview of Level-S^{2}fM.**

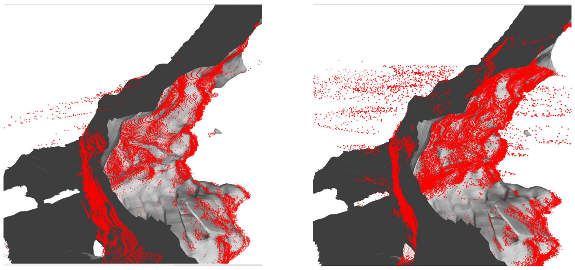
3D points by sphere tracing (with depth consistency)

3D points by sphere tracing (without depth consistency)

Figure 3. An illustrative comparison for the depth consistency loss $\mathcal{L}_{dc}$ in two-view initialization. As it is shown, when we remove $\mathcal{L}_{dc}$, the 3D points traced from all putative 2D keypoints correspondences will contain more flying 3D points.

volumetric rendering by

$$\mathcal{L}_{dc} = \frac{1}{B}\sum \|\hat{t}_i - \int_0^\infty T(t)\sigma(\mathbf{x}(t))dt\|, \tag{5}$$

where the rays $\mathbf{x}(t)$ are randomly sampled from the images, and those rays are also used to compute the color loss $\mathcal{L}_{\text{RGB}}$. For the computation of Eikonal loss $\mathcal{L}_{eik}$, all the 3D points visited by sphere tracing and dense ray marching are used.

In summary, our two-view initialization of Level-S^{2}fM computes the total loss $\mathcal{L}_{\text{total}}^{\text{init}}$ by

$$\mathcal{L}_{\text{total}}^{\text{init}} = \alpha_1\mathcal{L}_{\text{reproj}} + \alpha_2\mathcal{L}_{\text{rel}} + \alpha_3\mathcal{L}_{\text{rend}} + \alpha_4\mathcal{L}_{\text{dc}}, \tag{6}$$

where α_1, α_2, α_3, and α_4 are the hyperparameters and use ADAM optimizer to optimize the networks.

When the initialization is finished, we compute the two 3D points $\mathbf{X}$ and $\mathbf{X}'$ for each correspondence by sphere tracing for image I_a and I_b. For an accurate correspondence, $\|\mathbf{X} - \mathbf{X}'\|$ and their SDF values should be all small enough, thus providing a good criterion to check the putative matches to initialize the 3D point set $\mathcal{X}$ and the feature track set $\mathcal{T}$ for all the verified two-view correspondences.

4.2. New Frame Registration

For every newly added frame, we will first construct the 3D-2D correspondence from the existing pointset and its feature tracks. After that, we calculate a coarse pose of the new frame with the standard PnP algorithms [18], and then refine it with both the reprojection error and the rendering loss. The registration loss can be calculated as follow:

$$\mathcal{L}_{\text{Regist}} = \beta_1\mathcal{L}_{\text{reproj}} + \beta_2\mathcal{L}_{\text{rend}}, \tag{7}$$

where the β_1, β_2 are two hyper-parameters, and the $\mathcal{L}_{\text{reproj}}$ here are calculated by the 3D-2D correspondences.

In this optimization, the pose of the newly added frame, the SDF network, and the radiance field network are jointly optimized. While during the changes in the pose and SDF, the original location in the pointset will maybe not be the right one on the surface. For this problem, we design a Neural Bundle Adjustment (NBA) strategy to dynamically update the pointset with respect to the SDF after the points triangulation and refinement in the next section. Therefore, we leave the details of NBA in Sec. 4.4.

4.3. Points Triangulation and Refinement

Once the pose of the newly added frame is obtained, we step into the next procedure of refining the retrieved 2D points from the point set $\mathcal{X}$ and triangulating new 2D points into 3D space to extend $\mathcal{X}$. This problem was formulated in the classical SfM frameworks, however, they are suffering from the following issues:

- *The 2D Mismatches*: This issue could be alleviated by geometric verifications like RANSAC [8] or better

2D keypoint matching approaches, however, when encountering the symmetry structures or repeated texture regions, those efforts are hard to work efficiently.

- *Tiny Triangulation Angle*: This issue will lead to an ill-conditioned problem for points triangulation [13]. Therefore, the classical SfM approaches will directly discard those points to avoid the ill-conditioned problem configuration.

We address those issues by proposing an SDF-based triangulation. Similar to the two-view initialization in Sec. 4.1, we compute the 3D points for all the potential 2D keypoints in the first step. Then, for the 2D keypoints that have correspondences in the current feature track set $\mathcal{T}$, we use the tracing loss $\mathcal{L}_{\text{tracing}}$

$$\mathcal{L}_{\text{tracing}} = \frac{1}{V'} \sum_j \|\mathbf{X}_j^{st} - \mathbf{X}_j\|, \tag{8}$$

where $\mathbf{X}_j \in \mathcal{X}$ is the retrieved 3D point of the 2D keypoint in the current frame, V' is the number of retrieved 3D points. This loss function acts as the similar role of $\mathcal{L}_{dc}$ in two-view initialization. Without it, similar phenomenon like Fig. 3 will happen.

For the new 2D keypoints that are matched to the added images but without 3D information, both the reprojection loss similar to the two-view initialization and the tracing loss is used to yield the triangulation loss $\mathcal{L}_{\text{tri}}$ by

$$\mathcal{L}_{\text{tri}} = \mathcal{L}_{\text{reporj}}^{\text{mask}} + \mathcal{L}_{\text{tracing}}, \tag{9}$$

where $\mathcal{L}_{\text{reporj}}^{\text{mask}}$ only considers the 2D correspondences of which their distance between the 2D projections of the traced 3D points traced in different views are smaller than a loose threshold (45 pixels in our implementation).

4.4. Neural Bundle Adjustment on Surfaces

Because the camera pose estimation and the points triangulation are separated, which will involve accumulative errors for pose estimation and triangulation, as well as the implicit networks. Motivated by the Bundle Adjustment that is extensively used in classical approaches, we present a Neural Bundle Adjustment (NBA) that jointly optimizes the estimated camera points, the 3D point set, and the implicit networks as a refinement step. To avoid costly computation, our NBA step finds the closest surface points to dynamically update those variables.

Denoted by the reconstructed 3D point set $\mathcal{X}$ and the feature track $\mathcal{T}$, the camera poses $\mathcal{P} = \{P_1, \dots, P_K\}$ and the corresponding images $\{I_1, \dots, I_K\}$, as well as the networks $\phi(\mathbf{x})$ and L_ψ, in each step of NBA, we update the 3D point $\mathbf{X} \in \mathcal{X}$ by

$$\mathbf{X} \leftarrow \mathbf{X} - \phi(\mathbf{X}) \nabla \phi(\mathbf{X}), \tag{10}$$

and then compute the reprojection loss according to the feature track $\mathcal{T}$ to jointly optimize the ϕ the SDF network, $\mathcal{P}$ the estimated camera poses, and $\mathcal{X}$ the updated 3D point set. For the radiance network L_ψ, the rendering loss for randomly sampled rays is computed.

In our implementation, we leverage our NBA by three times, which we call the 1-frame NBA, local NBA, and global NBA. Because the rendering loss involves more rays, we only use it for the 1-frame NBA after the camera registration and point triangulation. In terms of local NBA, for the newly added view, only the related views with correspondences are considered. After running the 1-frame and local NBA schemes, we globally update all reconstructed views and the point set. By leveraging the backpropagation, all the mentioned variables are updated as the refinement.

5. Experiments

5.1. Implementation Details, Datasets, and Metrics

Implementation Details. In our implementation, we parameterize the SDF $\phi(\mathbf{x})$ by a multi-resolution features grid and a two-layers MLP. To accelerate the computation, we follow InstantNGP [28] to use a hash table [27] for the feature grids. The radiance field L_ψ is also implemented in a multi-resolution feature grid and a three-layer MLP. Because our end task is the geometric 3D reconstruction, we use a high-resolution multi-scale feature grid for the SDF to ensure the accuracy of scene geometry but use a low-resolution feature grid to avoid the unnecessary computation cost for the radiance field. The specifications of the network architecture are given in supplementary material due to the limited space. All of these above are implemented in PyTorch [32], and we used the Adam [17] as the optimizer for the geometric calculations. For the 2D image matching and pose graph, we keep them the same with our baseline, COLMAP [34] for fair comparisons.

Datasets. We use the BlendedMVS dataset in our evaluation because it provides accurate ground truth of camera poses and contains a number of challenging scenes for SfM. Because the BlendedMVS dataset is large-scale, we select 5 representative scenes including the *LyingStatue*, *Stone*, *Fountain*, *Horse*, and *Statues* in our experiments. Meanwhile, the DTU dataset for MVS task is also used. The five representative scenes (scans of 24, 37, 65, 110 and 114) are used in our experiments.

Evaluation Metrics. In our evaluation, we use the Rotation error and ATE to quantitatively benchmark the pose accuracy, which simply depicts the difference between the ground truth and the aligned pose. During our evaluation, we used the provided API of Reconstruction Align in COLMAP [34] to do that. In terms of the reconstructed scene geometry, we use accuracy (Acc) and the precision (Prec) rate to evaluate the accuracy of our recovered 3D

Scenes	Camera Pose Evaluation						Points Cloud Results Evaluation		
	Rotation (°) ↓			Translation (cm) ↓			Acc(cm)↓, Prec(≤3.5cm)↑		
	COLMAP [34]	Level-S^{2}fM (full)	Level-S^{2}fM (wo/render)	COLMAP [34]	Level-S^{2}fM (full)	Level-S^{2}fM (wo/render)	COLMAP [34]	Level-S^{2}fM (full)	Level-S^{2}fM (wo/render)
LyingStatue	1.20	1.12	1.31	0.89	2.18	2.67	**Acc**:0.83 **Prec**:0.99	**Acc**:1.35 **Prec**:0.99	**Acc**:1.76 **Prec**:0.98
Stone	0.63	0.31	0.54	6.28	5.51	9.17	**Acc**:5.44 **Prec**:0.66	**Acc**:3.61 **Prec**:0.68	**Acc**:5.04 **Prec**:0.64
Fountain	4.34	1.65	2.32	7.41	2.87	4.11	**Acc**:1.91 **Prec**:0.91	**Acc**:1.13 **Prec**:0.98	**Acc**:1.14 **Prec**:0.96
Horse	0.33	0.94	0.92	1.18	5.71	7.58	**Acc**:3.99 **Prec**:0.86	**Acc**:4.18 **Prec**:0.71	**Acc**:4.18 **Prec**:0.70
Statues	1.21	0.36	0.44	1.98	0.56	0.62	**Acc**:1.31 **Prec**:0.98	**Acc**:0.95 **Prec**:0.99	**Acc**:1.02 **Prec**:0.99
Mean	1.54	**0.86**	1.11	3.54	**3.36**	4.83	**Acc**:3.16 **Prec**:0.85	**Acc**:**2.25** **Prec: 0.87**	**Acc**:2.63 **Prec**:0.85

Table 1. **Quantitative results on the BlendedMVS dataset.** For our Level-S^{2}fM, we report the results by full version and an wo/render version that removes the rendering loss during optimization.

Pose Source	LyingStatue	Stone	Fountain	Horse	Statues	Mean
COLMAP	29.1	28.4	25.4	23.5	29.2	27.12
Level-S^{2}fM (Ours)	29.5	28.9	27.1	23.6	30.2	27.86
GT	29.5	29.4	27.4	24.1	31.1	28.3

Table 2. **Novel View Synthesis Comparison.** We report the average PSNR to compare the influence of the camera poses computed by COLMAP, Level-S^{2}fM and the GT poses on the BlendedMVS dataset.

points and Chamfer-$l1$ distance to depict the accuracy of the reconstructed surface. Detailed definitions of these evaluation metrics are given in the supplementary material.

5.2. Results on the BlendedMVS Dataset

Tab. 1 reports the quantitative evaluation results for the two versions of Level-S^{2}fM and COLMAP [34]. The full version of Level-S^{2}fM used all the mentioned components while the wo/render version removed the rendering loss for optimization. As it is reported, our Level-S^{2}fM (full) consistently outperforms COLMAP [34] for camera pose estimation and sparse 3D point cloud reconstruction. It also reveals that rendering losses are required.

In detail, our Level-S^{2}fM (full) averagely reduced the estimation error from 1.54° by COLMAP [34] to 0.86°, **obtaining a relative improvement of 55.84%.** For the translation error, our Level-S^{2}fM (full) decreases the error from 3.54 cm to 3.36 cm. For the sparse 3D point cloud reconstruction, the ACC metric is reduced from 3.16 to 2.25 for the full model and 2.63 for the wo/render version.

Fig. 4 shows the reconstruction results by our method.

Apart from the direct evaluation of the SfM results on the BlendedMVS dataset, we further compare the camera poses estimation results for different methods by training the NGP [28] (a fast version of NeRF [25]) to compare the performance of novel view synthesis in Tab. 2. As it is reported, the rendered images by our camera poses are consistently better than the ones by COLMAP poses.

Scan	COLMAP [34]			Level-S^{2}fM (Ours)		
	Chamfer-ℓ_1	Rot. Err.	Trans. Err.	Chamfer-ℓ_1	Rot. Err.	Trans. Err.
24	2.176	0.38	2.87	2.442	0.81	4.60
37	3.837	0.41	4.86	3.023	0.31	4.29
65	4.394	0.45	4.23	3.190	0.74	5.81
110	3.389	0.65	6.36	5.902	0.82	6.82
114	3.577	0.35	3.58	2.092	0.14	1.85
Mean	3.330	0.448	4.38	3.474	0.564	4.67

Table 3. **Quantitative results on DTU dataset.** The Chamfer-ℓ_1 distance of the dense reconstruction results and as the errors of rotation and translation for camera pose estimation, are compared for COLMAP and our Level-S^{2}fM. The unit of Chamfer-ℓ_1 and Translation errors are in millimetres.

5.3. Results on the DTU Dataset

We conducted the evaluation on the DTU to illustrate the promising future of our Level-S^{2}fM to unify the pose estimation, dense reconstruction, and novel view synthesis problems in one stage. For the comparison to COLMAP, we use their built-in PatchMatch MVS [35] functionality to obtain the dense surface points and then leverage its default surface reconstruction method (*i.e.*, Poisson surface [16]) to obtain the mesh model. For our Level-S^{2}fM, we use the MarchingCubes [21] to extract the mesh models from the zero-level set of the implicit surface. The quantitative evaluation results are shown in Tab. 3. In this dataset, our Level-S^{2}fM obtains on-par performance with COLMAP.

5.4. Limitations of Level-S^{2}fM

In order to explore the clear boundary of Level-S^{2}fM and point out the potential future development, we discuss the limitation of Level-S^{2}fM on the most typical indoor dataset, scannet [6]. In the Scannet [6], there are a lot of challenges including blurry images, and textureless areas. Because of the less texture, the SIFT-based keypoint correspondences may contain a large portion of outliers or insufficient matches. Meanwhile, the blur in images will also influence the accuracy of the 2d matches. Therefore, most SfM easily fails on this dataset. Our method is also limited by this because of SIFT matches.

To make the discussion clear, we run four scenes of

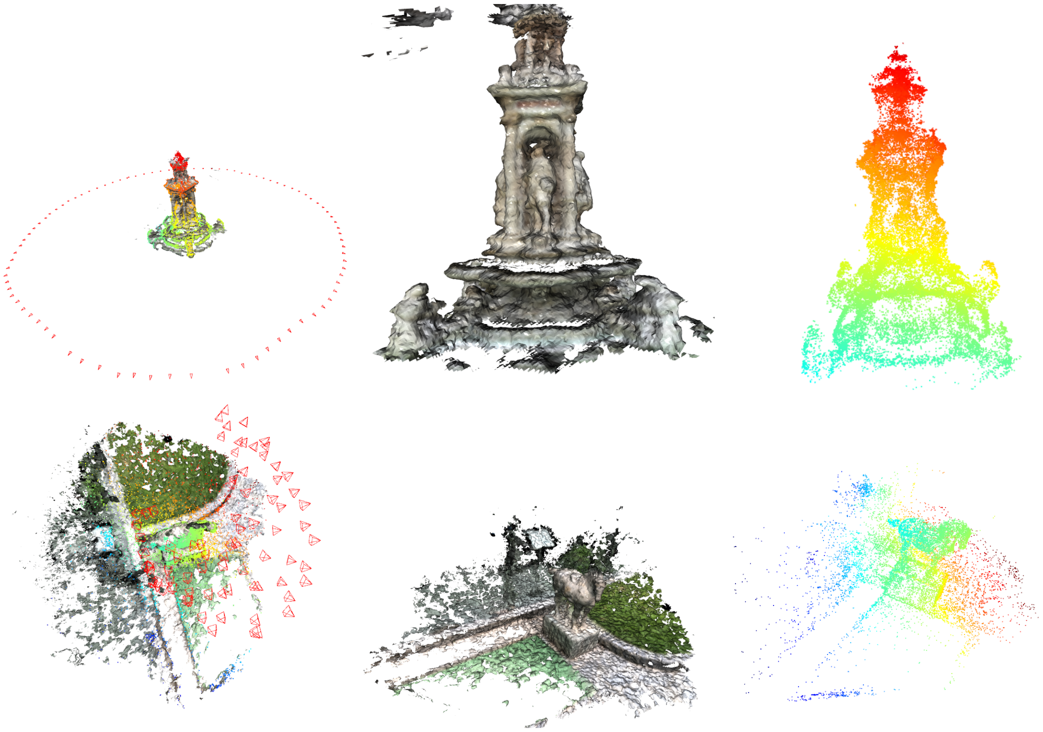

Figure 4. The reconstructed meshes, point clouds and camera poses for the *Fountain* and *Horse* scenes on the BlendedMVS dataset by our Level-S^{2}fM (full). In the first column, the reconstructed scene geometry and the camera poses are shown together. For the 3D models, we show the different views of the sparse 3D points during the training and the textured meshes refused from the zero-level set surface.

Scene ID		0000	0059	0169	0207
iMAP [38]	rot°↓	–	–	–	–
	trans. (cm) ↓	197.1	18.9	96.4	28.7
NICESLAM [48]	rot°↓	–	–	–	–
	trans. (cm) ↓	11.3	12.0	12.0	12.8
COLMAP [34]	rot°↓	1.47/2.71/2.71	1.40/2.52/2.66	2.64/1.84/2.52	failed
	trans. (cm) ↓	8.20/16.8/14.1	7.20/10.8/11.5	10.6/9.22/10.6	–
Level-S^{2}fM	rot°↓	1.44/2.23/1.98	1.50/2.59/3.72	2.94/9.09/14.3	failed
full	trans. (cm) ↓	6.50/11.8/26.7	8.20/32.9/35.7	6.35/14.3/44.8	–

Table 4. **Quantitative results** of pose estimation on ScanNet [6]. For the COLMAP and Level-S^{2}fM, we report their pose accuracy metrics when the 60/120/all frames are registered. For the last scene (*i.e.*, 0207), both COLMAP and our method failed.

Scannet [6] that were used for NICESLAM [48]. For the image sequence of each scene, the input image set for SfM is constructed by sampling for every 10 frames. Tab. 4 reports the pose accuracy of COLMAP and our Level-S^{2}fM for results by adding 60 frames, 120 frames, and all the frames, which are concatenated by the "slash". As it is reported, our method usually performs well in the first 60 frames but its pose estimation accuracy suddenly decreases when adding some new frames. The textureless matches cause the matches very sparse and therefore hard to give a good registration of images. Meanwhile, since the radiance field learning is also challenging in the Scannet dataset, the bad initialized pose can not be refined well by the rendering loss. All of these limitations are basically from sparse 2D image matches. Besides, we observed that the ADAM optimizer will make the optimization of camera poses and scene points unstable, which would also affect the final results.

6. Conclusion

This paper studies the longstanding problem of Structure-from-Motion by exploring and exploiting several important yet challenging issues including the two-view neural rendering in the initialization stage and few-view neural rendering in the early camera registration stage of incremental SfM for integrating the recent advances of neural implicit field learning into an SfM pipeline. We show that although the few-view neural rendering problem is challenging enough, it can be tackled by the 2D correspondences as they convey strong inductive biases for 3D scenes. Based on this, we present the first neural SfM solution that renews several key components of two-view geometry initialization, camera pose registration, and triangulation, as well as the Bundle Adjustment problem with neural implicit fields. In the experiments, we show that Level-S^{2}fM outperforms the traditional SfM pipeline and set a new state-of-the-art for 3D reconstruction on the BlendedMVS dataset. We believe that our study will encourage the 3D vision community to rethink and reformulate Structure-from-Motion with learning-based new findings.

References

[1] Jonathan T. Barron, Ben Mildenhall, Matthew Tancik, Peter Hedman, Ricardo Martin-Brualla, and Pratul P. Srinivasan. Mip-nerf: A multiscale representation for anti-aliasing neural radiance fields. In *ICCV*, pages 5835–5844. IEEE, 2021. 3

[2] Ronald Clark. Volumetric bundle adjustment for online photorealistic scene capture. In *CVPR*, pages 6114–6122. IEEE, 2022. 3

[3] Ronald Clark, Michael Bloesch, Jan Czarnowski, Stefan Leutenegger, and Andrew J. Davison. Learning to solve nonlinear least squares for monocular stereo. In *ECCV*, volume 11212, pages 291–306, 2018. 2

[4] David J. Crandall, Andrew Owens, Noah Snavely, and Daniel P. Huttenlocher. Sfm with mrfs: Discrete-continuous optimization for large-scale structure from motion. *IEEE Trans. Pattern Anal. Mach. Intell.*, 35(12):2841–2853, 2013. 1

[5] Hainan Cui, Xiang Gao, Shuhan Shen, and Zhanyi Hu. Hsfm: Hybrid structure-from-motion. In *CVPR*, pages 2393–2402, 2017. 1

[6] Angela Dai, Angel X. Chang, Manolis Savva, Maciej Halber, Thomas A. Funkhouser, and Matthias Nießner. Scannet: Richly-annotated 3d reconstructions of indoor scenes. In *CVPR*, pages 2432–2443, 2017. 7, 8, 13

[7] Daniel DeTone, Tomasz Malisiewicz, and Andrew Rabinovich. Superpoint: Self-supervised interest point detection and description. In *CVPRW*, pages 224–236, 2018. 2, 13

[8] Martin A Fischler and Robert C Bolles. Random sample consensus: a paradigm for model fitting with applications to image analysis and automated cartography. *Communications of the ACM*, 24(6):381–395, 1981. 5

[9] Clément Godard, Oisin Mac Aodha, Michael Firman, and Gabriel J. Brostow. Digging into self-supervised monocular depth estimation. In *ICCV*, pages 3827–3837. IEEE, 2019. 3

[10] John C. Hart. Sphere tracing: a geometric method for the antialiased ray tracing of implicit surfaces. *Vis. Comput.*, 12(10):527–545, 1996. 3, 4

[11] Herman O Hartley. The modified gauss-newton method for the fitting of non-linear regression functions by least squares. *Technometrics*, 3(2):269–280, 1961. 13

[12] Richard Hartley and Andrew Zisserman. *Multiple view geometry in computer vision*. Cambridge university press, 2003. 1

[13] Richard I Hartley and Peter Sturm. Triangulation. *Computer vision and image understanding*, 68(2):146–157, 1997. 6

[14] Petr Hruby, Timothy Duff, Anton Leykin, and Tomás Pajdla. Learning to solve hard minimal problems. In *CVPR*, pages 5522–5532. IEEE, 2022. 2

[15] Rasmus Ramsbøl Jensen, Anders Lindbjerg Dahl, George Vogiatzis, Engin Tola, and Henrik Aanæs. Large scale multi-view stereopsis evaluation. In *CVPR*, pages 406–413. IEEE Computer Society, 2014. 2, 13

[16] Michael M. Kazhdan, Matthew Bolitho, and Hugues Hoppe. Poisson surface reconstruction. In Alla Sheffer and Konrad Polthier, editors, *Proceedings of the Fourth Eurographics Symposium on Geometry Processing*, volume 256 of *ACM International Conference Proceeding Series*, pages 61–70. Eurographics Association, 2006. 7

[17] Diederik P Kingma and Jimmy Ba. Adam: A method for stochastic optimization. In *ICLR (Poster)*, 2015. 6, 13

[18] Vincent Lepetit, Francesc Moreno-Noguer, and Pascal Fua. Ep*n*p: An accurate $O(n)$ solution to the p*n*p problem. *Int. J. Comput. Vis.*, 81(2):155–166, 2009. 5

[19] Chen-Hsuan Lin, Wei-Chiu Ma, Antonio Torralba, and Simon Lucey. BARF: bundle-adjusting neural radiance fields. In *ICCV*, pages 5721–5731, 2021. 2, 3

[20] Shaohui Liu, Yinda Zhang, Songyou Peng, Boxin Shi, Marc Pollefeys, and Zhaopeng Cui. DIST: rendering deep implicit signed distance function with differentiable sphere tracing. In *CVPR*, pages 2016–2025, 2020. 2, 4, 12

[21] William E. Lorensen and Harvey E. Cline. Marching cubes: A high resolution 3d surface construction algorithm. pages 163–169. ACM, 1987. 7

[22] David G Lowe. Distinctive image features from scale-invariant keypoints. *International journal of computer vision*, 60(2):91–110, 2004. 4

[23] Reza Mahjourian, Martin Wicke, and Anelia Angelova. Unsupervised Learning of Depth and Ego-Motion From Monocular Video Using 3D Geometric Constraints. In *CVPR*, pages 5667–5675. Computer Vision Foundation / IEEE Computer Society, 2018. 3

[24] Ishit Mehta, Manmohan Chandraker, and Ravi Ramamoorthi. A level set theory for neural implicit evolution under explicit flows. In *ECCV*, 2022. 2

[25] Ben Mildenhall, Pratul P. Srinivasan, Matthew Tancik, Jonathan T. Barron, Ravi Ramamoorthi, and Ren Ng. Nerf: Representing scenes as neural radiance fields for view synthesis. In Andrea Vedaldi, Horst Bischof, Thomas Brox, and Jan-Michael Frahm, editors, *ECCV*, volume 12346, pages 405–421, 2020. 2, 3, 7, 13

[26] Jorge J Moré. The levenberg-marquardt algorithm: implementation and theory. In *Numerical analysis*, pages 105–116. Springer, 1978. 13

[27] Thomas Müller. tiny-cuda-nn, 4 2021. 6

[28] Thomas Müller, Alex Evans, Christoph Schied, and Alexander Keller. Instant neural graphics primitives with a multiresolution hash encoding. *ACM Trans. Graph.*, 41(4):102:1–102:15, 2022. 6, 7, 10

[29] David Nistér. An Efficient Solution to the Five-Point Relative Pose Problem. *IEEE TPAMI*, 26(6):756–777, 2004. 4, 12

[30] Michael Oechsle, Songyou Peng, and Andreas Geiger. UNISURF: unifying neural implicit surfaces and radiance fields for multi-view reconstruction. In *ICCV*, pages 5569–5579, 2021. 3

[31] Jeong Joon Park, Peter Florence, Julian Straub, Richard A. Newcombe, and Steven Lovegrove. Deepsdf: Learning continuous signed distance functions for shape representation. In *CVPR*, pages 165–174, 2019. 3

[32] Adam Paszke, Sam Gross, Francisco Massa, Adam Lerer, James Bradbury, Gregory Chanan, Trevor Killeen, Zeming Lin, Natalia Gimelshein, Luca Antiga, Alban Desmai-

son, Andreas Köpf, Edward Z. Yang, Zachary DeVito, Martin Raison, Alykhan Tejani, Sasank Chilamkurthy, Benoit Steiner, Lu Fang, Junjie Bai, and Soumith Chintala. Pytorch: An imperative style, high-performance deep learning library. In *NeurIPS*, pages 8024–8035, 2019. 6

[33] Paul-Edouard Sarlin, Daniel DeTone, Tomasz Malisiewicz, and Andrew Rabinovich. Superglue: Learning feature matching with graph neural networks. In *CVPR*, pages 4937–4946. Computer Vision Foundation / IEEE, 2020. 2, 13

[34] Johannes L Schönberger and Jan-Michael Frahm. Structure-from-motion Revisited. In *CVPR*, pages 4104–4113, 2016. 1, 2, 3, 4, 6, 7, 8, 11, 13

[35] Johannes L. Schönberger, Enliang Zheng, Jan-Michael Frahm, and Marc Pollefeys. Pixelwise view selection for unstructured multi-view stereo. In *ECCV*, volume 9907, pages 501–518. Springer, 2016. 7

[36] Noah Snavely, Steven M. Seitz, and Richard Szeliski. Skeletal graphs for efficient structure from motion. In *CVPR*, 2008. 4

[37] Jürgen Sturm, Nikolas Engelhard, Felix Endres, Wolfram Burgard, and Daniel Cremers. A benchmark for the evaluation of RGB-D SLAM systems. In *2012 IEEE/RSJ International Conference on Intelligent Robots and Systems*, pages 573–580. IEEE, 2012. 11

[38] Edgar Sucar, Shikun Liu, Joseph Ortiz, and Andrew J. Davison. imap: Implicit mapping and positioning in real-time. In *ICCV*, pages 6209–6218. IEEE, 2021. 3, 8, 13

[39] Chengzhou Tang and Ping Tan. Ba-net: Dense bundle adjustment networks. In *7th International Conference on Learning Representations, ICLR 2019, New Orleans, LA, USA, May 6-9, 2019*, 2019. 2

[40] Jianyuan Wang, Yiran Zhong, Yuchao Dai, Stan Birchfield, Kaihao Zhang, Nikolai Smolyanskiy, and Hongdong Li. Deep two-view structure-from-motion revisited. In *CVPR*, pages 8953–8962. Computer Vision Foundation / IEEE, 2021. 2

[41] Lei Wang, Linlin Ge, Shan Luo, Zihan Yan, Zhaopeng Cui, and Jieqing Feng. Tc-sfm: Robust track-community-based structure-from-motion. *CoRR*, abs/2206.05866, 2022. 2

[42] Peng Wang, Lingjie Liu, Yuan Liu, Christian Theobalt, Taku Komura, and Wenping Wang. Neus: Learning neural implicit surfaces by volume rendering for multi-view reconstruction. In *NeurIPS*, pages 27171–27183, 2021. 3

[43] Yiqun Wang, Ivan Skorokhodov, and Peter Wonka. Improved surface reconstruction using high-frequency details. *CoRR*, abs/2206.07850, 2022. 3

[44] Zirui Wang, Shangzhe Wu, Weidi Xie, Min Chen, and Victor Adrian Prisacariu. Nerf-: Neural radiance fields without known camera parameters. *CoRR*, abs/2102.07064, 2021. 2, 3

[45] Kyle Wilson and Noah Snavely. Robust global translations with 1dsfm. In *ECCV*, volume 8691, pages 61–75, 2014. 1

[46] Yao Yao, Zixin Luo, Shiwei Li, Jingyang Zhang, Yufan Ren, Lei Zhou, Tian Fang, and Long Quan. Blendedmvs: A large-scale dataset for generalized multi-view stereo networks. In *CVPR*, pages 1787–1796, 2020. 2

[47] Lior Yariv, Jiatao Gu, Yoni Kasten, and Yaron Lipman. Volume rendering of neural implicit surfaces. In Marc'Aurelio Ranzato, Alina Beygelzimer, Yann N. Dauphin, Percy Liang, and Jennifer Wortman Vaughan, editors, *NeurIPS*, pages 4805–4815, 2021. 3, 4

[48] Zihan Zhu, Songyou Peng, Viktor Larsson, Weiwei Xu, Hujun Bao, Zhaopeng Cui, Martin R. Oswald, and Marc Pollefeys. NICE-SLAM: neural implicit scalable encoding for SLAM. In *CVPR*, pages 12776–12786. IEEE, 2022. 3, 8, 13

A. Network Architecture Details

The architecture of our Level-S^{2}fM is shown in Fig. 5. We use dual fields to independently represent the radiance field and signed distance field (SDF), which have the same architecture. For each queried 3d point, we will first interpolate the feature of the queried points at multi-resolution grids, and then concatenate the multi-resolution features into the MLP to attain the density or the radiance. To accelerate the training, we adopt the multi-resolution hash table [28] in our implementation. In detail, we construct multiresolution grids of L levels, and the resolution of each level is:

$$N_l := \lfloor N_{min} \cdot b^l \rfloor \,, \tag{11}$$

$$b := \exp\left(\frac{\ln N_{max} - \ln N_{min}}{L-1}\right) \,, \tag{12}$$

where N_{min} and N_{max} are the coarsest and finest resolutions. In the multi-resolution hash table, to obtain the feature of point $\mathbf{x}$, we first scale and round $\mathbf{x}$ at each level l as $\lfloor \mathbf{x}_l \rfloor = \lfloor \mathbf{x} \cdot N_l \rfloor$, $\lceil \mathbf{x}_l \rceil = \lceil \mathbf{x} \cdot N_l \rceil$. Then we can obtain the voxel spanned by $\lfloor \mathbf{x}_l \rfloor$ and $\lceil \mathbf{x}_l \rceil$ and map each corner of the voxel to the hash table using the spatial hash function:

$$h(\mathbf{x}) = \left(\bigoplus_{i=1}^{3} x_i \pi_i \right) \mod T \,, \tag{13}$$

where $\oplus$ denotes the bit-wise XOR operation, and π_i are unique, large prime numbers. In our implementation, π_1, π_2, π_3 and T are set to $1, 2654435761, 805459861, 2^{19}$ respectively. After that, the feature vectors at each corner are interpolated at $\mathbf{x}$ by the interpolation weight $\mathbf{w}_l = \mathbf{x}_l - \lfloor \mathbf{x}_l \rfloor$. Lastly, we concatenate the feature vector of $\mathbf{x}$ at each level, as well as the encoded view direction $\mathbf{v}$ togehter, and send it into an MLP to predict the values. In our implementation, we leverage two different resolution hash tables to represent the sdf and radiance fields respectively. For sdf function, the configuration is $L = 8, N_{min} = 16, N_{max} = 2048$ and the number of features at each level is 4. While the configuration for radiance field is $L = 16, N_{min} = 16, N_{max} = 2048$ and the number of features at each level is 2.

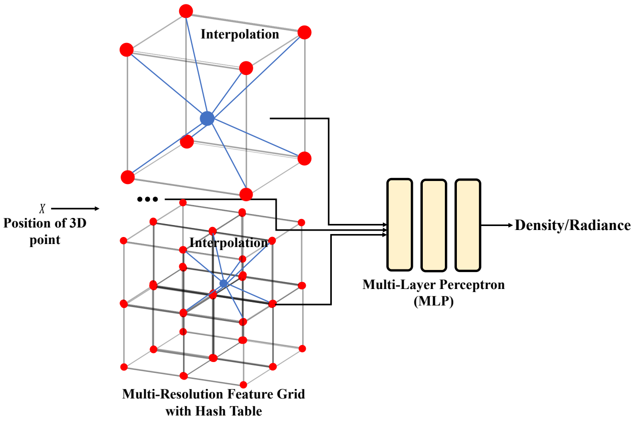
Interpolation
x Position of 3D point
Interpolation
Density/Radiance
Multi-Layer Perceptron (MLP)
Multi-Resolution Feature Grid with Hash Table

Figure 5. **The Multi-resolution Features Grid.**

B. Evaluation Metrics and Details

Because the world coordinate system varies for different SfM systems, we need to align the estimated poses to the ground truth poses first. We use the reconstruction alignment API from COLMAP [34], which first pre-aligns the two reconstructions with their poses and refine that by aligning the sparse point clouds of them. Here, the sparse point clouds are triangulated by the 2d matches of SIFT with the fixed poses, which can be also easily implemented with the existing COLMAP API. After the alignment, the rotation error is computed as follows:

$$\theta_i^{\text{error}} = \cos^{-1}\frac{\text{trace}(\mathbf{R}_i^{\text{gt}}\hat{\mathbf{R}}_i^T) - 1}{2}, i = \{1, ..., M\}, \quad (14)$$

where the M is the number of the cameras, and $\mathbf{R}_i^{\text{gt}}$, $\hat{\mathbf{R}_i}^T$ are the gt rotation matrix and aligned estimated rotation matrix respectively. We take the average error of the rotation in Equation (14) as the metric for rotation. As for the evaluation of translation, we use the ATE RMSE [37] to depict the distance between the ground truth trajectories and the estimated, specifically followed:

$$\text{RMSE}(\hat{\mathbf{T}}_i) = \left(\frac{1}{M}\sum_{i=0}^{M}||\text{trans}(\mathbf{T}_i^{-1}\hat{\mathbf{T}}_i)||^2\right)^{\frac{1}{2}}, \quad (15)$$

where the $\mathbf{T}_i, \hat{\mathbf{T}}_i$ are the gt and aligned transformation matrix respectively, and the trans means to take the translation part of the transformation matrix.

For the evaluation of reconstruction results, the definitions of metrics are shown in Table. 5. We use these two metrics to evaluate the accuracy of the reconstructed point cloud.

C. Two View Initialization

Because the learning of neural implicit fields was originally designed for bounded scenes, we have to carefully design the two-view initialization for our Level-S^{2}fM and ensure the incremental reconstruction process is within the bound. In our study, we mainly focus on two representative types of scenes. The first type is the inside-forward scene,

Metric	Definition
Acc	$\text{mean}_{p\in P}(\text{min}_{p^*\in P^*}\|\|p{-}p^*\|\|)$
Prec	$\text{mean}_{p\in P}(\text{min}_{p^*\in P^*}\|\|p{-}p^*\|\|{\le}.035)$

Table 5. Caption

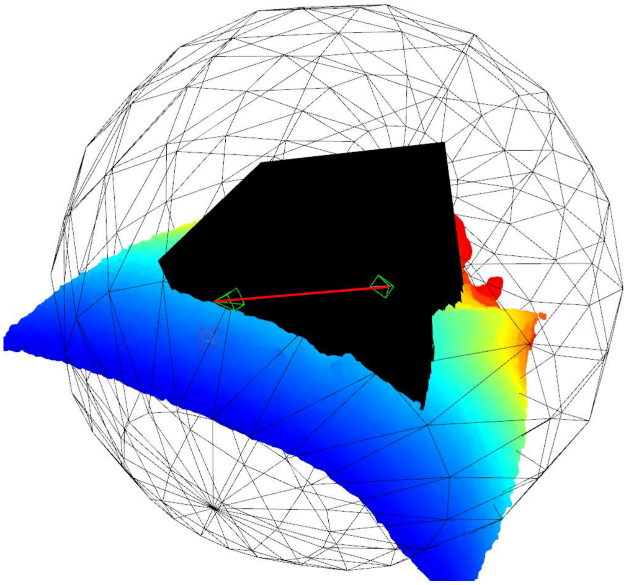

Figure 6. **The Visualization of Two View Initialization for Inside-forward Scenes.**

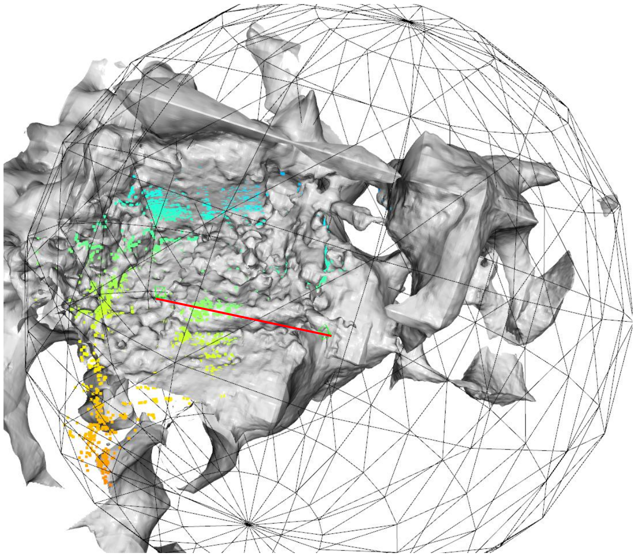

Figure 7. **The Visualization of Two View Initialization for Outside-forward Scenes.**

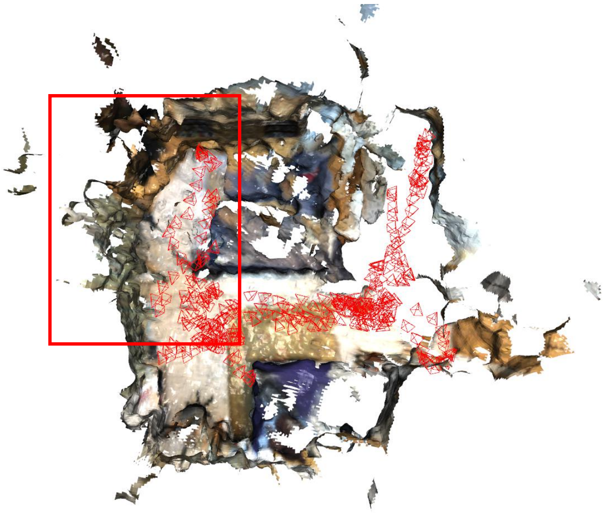

Figure 8. **Visualization of Mesh and Trajectory for Failure Cases.**This figure show the visualization of mesh and trajectory in scannet. As we can see the pose and geometry begin to be bad in the red box where the texture and matches are mostly less.

where the cameras are surrounded by the target object and inside forwarding (Specifically seen in Figure. 6). The second type is the outside-forward scenes. In initialization details for inside-forward scenes, we put the first camera on a sphere with $r = 3$, and orient the camera toward the origin of the coordinate. The bound of the features grid is set to $[4, 4, 4]$. The initialized pose for the first camera is calculated by the following:

$$\begin{aligned} \mathbf{t}_{\text{w2c}}^{\text{init}} &= \mathbf{R}_{\text{w2c}}^{\text{init}} \mathbf{t}_{\text{c2w}}^{\text{init}}, \\ \mathbf{t}_{\text{c2w}}^{\text{init}} &= \begin{bmatrix} -r\cos\theta_y\cos\theta_z \\ -r\cos\theta_y\sin\theta_z \\ -r\sin\theta_y \end{bmatrix}, \\ \mathbf{R}_{\text{w2c}}^{\text{init}} &= \mathbf{R}_x(\theta_x)^{-1}\mathbf{R}_{\mathbf{y}}(\theta_{\mathbf{y}})^{-1}\mathbf{R}_z(\theta_z)^{-1}, \end{aligned} \tag{16}$$

where the $\theta_x = 0, \theta_y = -\frac{1}{4}\pi, \theta_z = \frac{1}{4}\pi$. After that, the pose of the second camera is then initialized with the calculated relative pose by five points algorithm [29]. Meanwhile, the length of the translation of the relative pose would be the hyper-parameter for different scenes. As shown in Figure. 6, the red line is the baseline of the two-view camera, and the length of the baseline is empirically set. Moreover, for the outside-forward scene, the θ_x is set to $\frac{1}{2}\pi$ to make the orientation of the camera outside. It needs to be noticed that the specific parameters of two-view initialization may be different for different scenes, which can be referred into our codes and configuration after it is released.

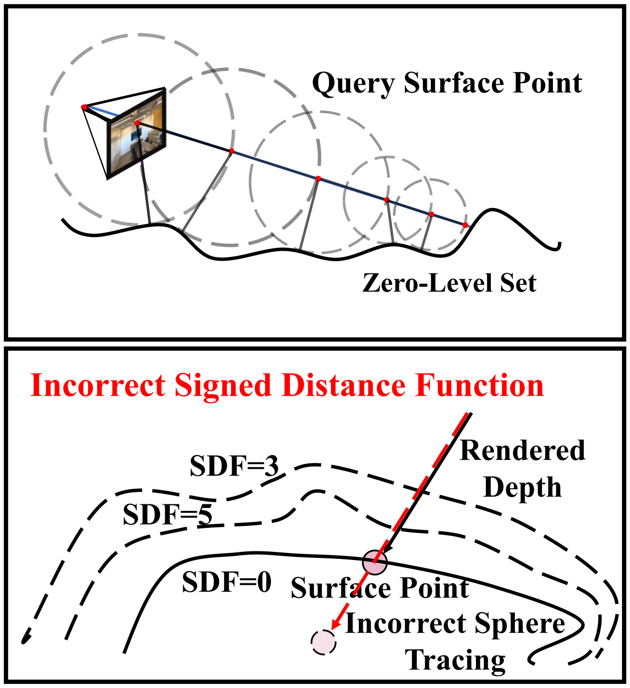

Figure 9. **Sphere Tracing and Depth Consistency.**

D. Sphere Tracing and Depth Consistency

As mentioned in our paper, the key component for attaining the 3D points from the 2D keypoints is sphere tracing. As shown in Figure. 9, sphere tracing algorithm [20] leverages the basic property of the signed distance function where the queried SDF value at each position is the closest distance from the point to the zero-level set of the surface. The depth of the queried 2d points can be calculated as follows:

$$\begin{aligned} \hat{t} &= t_0 + \sum_{j}^{max} sdf(\mathbf{X}_j), \\ X_{j+1} &= X_j + sdf(X_j)d, \end{aligned} \tag{17}$$

where the start point $X_0 = o + t_0 d$. By the sphere tracing algorithm, we can efficiently get the 3d points from 2d, and it can be a natural constraint for the learning of SDF. But sometimes, sphere tracing can not correctly trace the surface when the zero-level set is correct while non-zero-level sets are wrong. Therefore, it can not ensure the multi-view consistency of the sphere tracing algorithm (seen in the second row of Figure. 9). To overcome that, we use the depth calculated by volumetric rendering as a constraint to keep the consistency between these two sampling strategies as mentioned in our paper.

Scene		DTU [15]
Order 1st	rot°↓	0.74
	trans. (mm) ↓	5.81
Order 2nd	rot°↓	0.30
	trans. (mm) ↓	2.04

Table 6. **Ablation for Sequence Order.**

E. Sequence Order for Incremental Reconstruction

For incremental SfM, the sequence order for incremental reconstruction is a relatively important component of the final result. But this paper concentrates our attention into renew the SfM on the neural level sets, which show its promising future to make breakthroughs. To avoid being exhausted to be stuck in the discussion of various tricks and strategies, we simply implement the next best view selection according to the number of 3D-2D pairs in PnP which may have a better alternative discussed in [34]. In order completely discuss our framework, we also report the simple ablation result for the sequence order in Level-S^{2}fM, which can be seen in Table. 6. We conducted the ablation study for sequence order in DTU [15]. We report two different sequence orders by randomly selecting the start of two frames for the two-view initialization. We can see that different sequence orders will cause different results. Despite of this, we would like to emphasize again that because of the complexity of Structure-from-Motion, the problem of the next-best view is not the core of our current study, which will be left in our future work.

F. More Qualitative Results on Individual Datasets

We also report more qualitative results for our experiments. In Figure. 11, there are the rendered image results from our radiance field. While, in Figure. 10, the estimated pose, reconstructed 3d points, and the mesh are visualized.

G. Discussion on Failure Cases

In our paper, we take the indoor datasets, ScanNet [6] to discuss our failure cases, where there are a lot of textureless regions. As shown in Figure. 12, because of the textureless areas or the blurry problem of the captured images, the 3D-2D correspondences are badly distributed and limited in number. Therefore, the registration of these images is hard to solve and results in bad initialization for the pose estimation. As seen in Figure. 8, the trajectory of cameras becomes unsatisfactory due to the textureless wall. Meanwhile, due to the incremental reconstruction fashion, the subsequent pose is based on the former, so, the incorrect pose estimation results by the textureless region will influence the whole process. To alleviate the problem, the recent robust deep learning-based 2d matches method may play a core role [7, 33], which will be our future works to explore the solution to this problem.

Meanwhile, for those NeRF [25] based SLAMs Framework [38, 48], they usually need the depth as an extra input. With the assistance of the depth map, the coarse pose is easily attained by aligning the depth of two consecutive frames, and they are not easily influenced by the issue of textureless. Therefore, in our paper, we did not compare our method with the depth-aware SLAM methods. Besides, we find that the optimizer for the networks is another core for getting stable and accurate pose results. The optimizer, Adam [17], used in our paper is may not the best choice for our problem as it is not easy to judge whether the optimization is converged. Therefore, in our future work, we are going to explore using the second-order optimizer like Levenberg-Marquardt (LM) [26] or Gauss-Newton (GN) [11] algorithm to solve our problem.

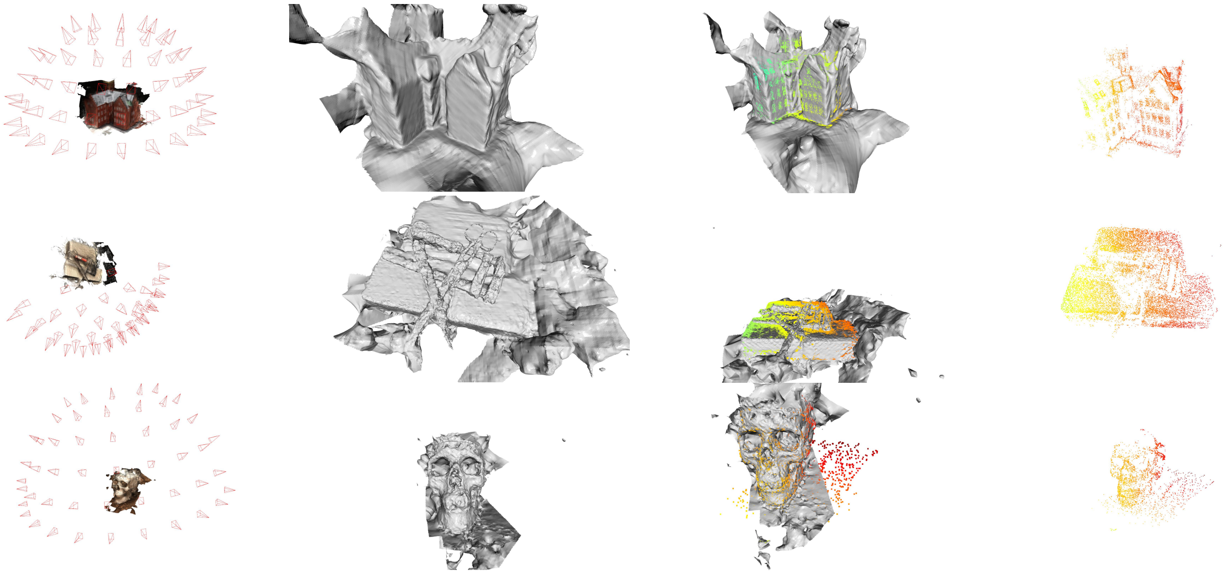

Figure 10. **Qualitative Results for Reconstruction and Pose Estimation.** The first column is the refused mesh and the visualization of camera poses. While, the second and third are the mesh and mesh shown with the points respectively. We can observe that our reconstructed points sticking on the surface of mesh. In the last column is the point cloud reconstructed.

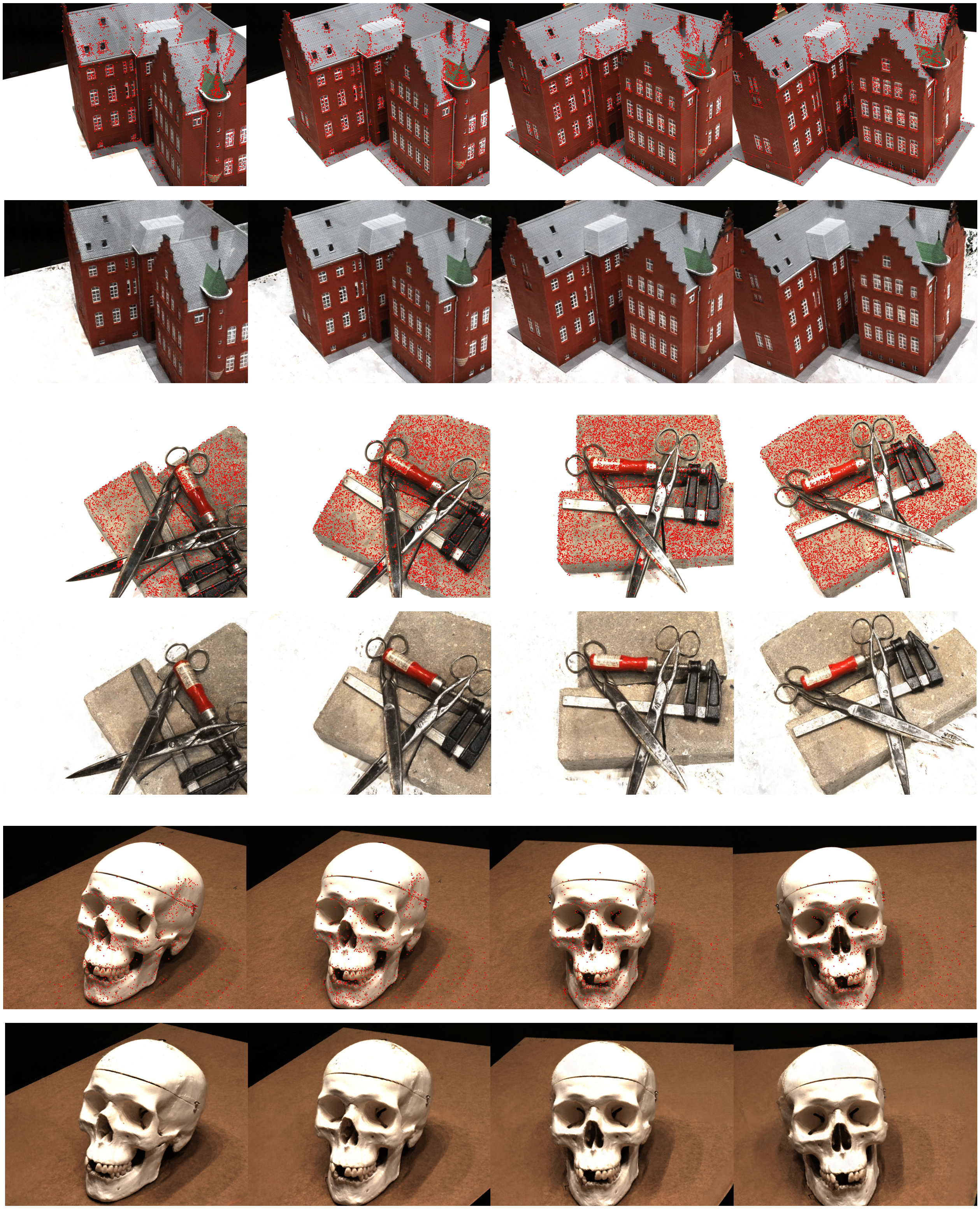

Figure 11. **Qualitative Results for Rendering.**This figure show the visualization of three scenes. At each group, the first row is the ground truth rgb images and their corresponded 3d observation projected on them. And the second row is the rendered images.

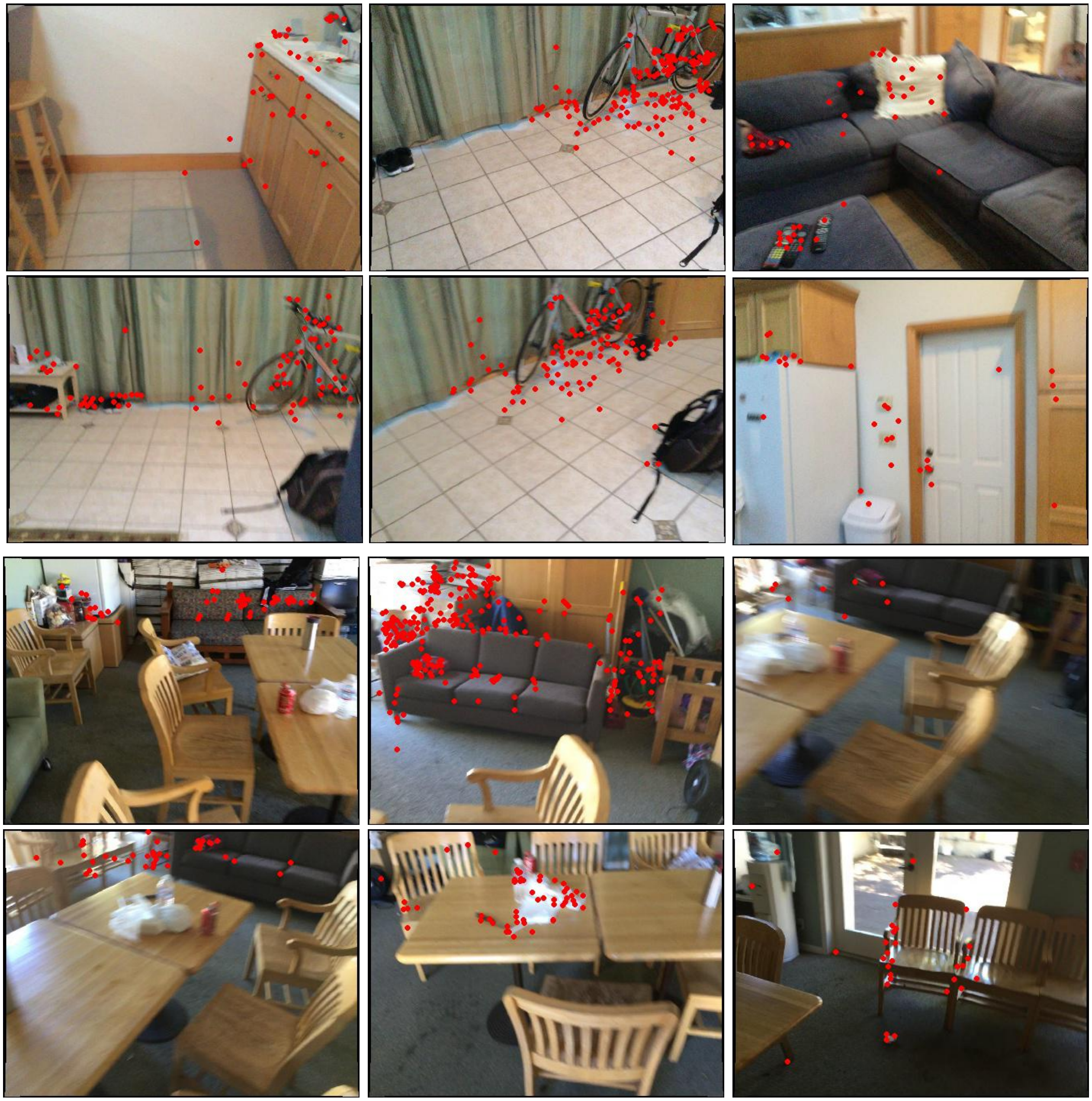

Figure 12. **Visualization for Images with Its 3D observations for PnP in Scannet.**This figure show that because of the blurry problem and textureless region, the 3D-2D correspondences are badly distributed and limited number.